ARO 22360.4-EG-S

(2)

ROTATING FLOW IN RADIAL TURBOMACHINERY

Final Report

T.R. Govindan, F.J. de Jong, W.R. Briley, and H. McDonald

May, 1990

U.S. Army Research Office
Contract DAAG29-85-C-0030

Co

Scientific Research Associates, Inc.
Glastonbury, CT 06033

Approved for Public Release;
Distribution Unlimited

[illegible] 142

UNCLASSIFIED MASTER COPY - FOR REPRODUCTION PURPOSES

SECURITY CLASSIFICATION OF THIS PAGE

REPORT DOCUMENTATION PAGE

1a. REPORT SECURITY CLASSIFICATION
Unclassified

1b. RESTRICTIVE MARKINGS

2a. SECURITY CLASSIFICATION AUTHORITY

2b. DECLASSIFICATION / DOWNGRADING SCHEDULE

3. DISTRIBUTION / AVAILABILITY OF REPORT
Approved for public release;
distribution unlimited.

4. PERFORMING ORGANIZATION REPORT NUMBER(S)
R930011-F

5. MONITORING ORGANIZATION REPORT NUMBER(S)
ARO 22360.4-EG-S

6a. NAME OF PERFORMING ORGANIZATION
Scientific Research Associates, Inc.

6b. OFFICE SYMBOL (If applicable)
8N189

7a. NAME OF MONITORING ORGANIZATION
U. S. Army Research Office

6c. ADDRESS (City, State, and ZIP Code)
50 Nye Road, P.O. Box 1058
Glastonbury, CT 06033

7b. ADDRESS (City, State, and ZIP Code)
P. O. Box 12211
Research Triangle Park, NC 27709-2211

8a. NAME OF FUNDING / SPONSORING ORGANIZATION
U. S. Army Research Office

8b. OFFICE SYMBOL (If applicable)

9. PROCUREMENT INSTRUMENT IDENTIFICATION NUMBER
DAAG29-85-C-0030

8c. ADDRESS (City, State, and ZIP Code)
P. O. Box 12211
Research Triangle Park, NC 27709-2211

10. SOURCE OF FUNDING NUMBERS

PROGRAM ELEMENT NO.	PROJECT NO.	TASK NO.	WORK UNIT ACCESSION NO.

11. TITLE (Include Security Classification)
Rotating Flow in Radial Turbomachinery

12. PERSONAL AUTHOR(S) T.R Govindan, F.J. De Jong, W.R. Briley and H. McDonald

13a. TYPE OF REPORT
Final

13b. TIME COVERED
FROM 10/85 TO 2/90

14. DATE OF REPORT (Year, Month, Day)
90/05

15. PAGE COUNT

16. SUPPLEMENTARY NOTATION The view, opinions and/or findings contained in this report are those of the author(s) and should not be construed as an official Department of the Army position, policy, or decision, unless so designated by other documentation.

17. COSATI CODES

FIELD	GROUP	SUB-GROUP

18. SUBJECT TERMS (Continue on reverse if necessary and identify by block number)

19. ABSTRACT (Continue on reverse if necessary and identify by block number)

The present study addresses the development and implementation of computational procedures for analysis and prediction of flows in centrifugal impellers. Two approaches have been investigated: (a) solution of the Navier-Stokes equations, and (b) solution of an approximate set of viscous primary/secondary flow equations by an efficient spatial marching algorithm. Solution of the Navier-Stokes equations has been directed towards computing the flow field in a rotating centrifugal impeller passage. Computed results show all the flow features of measurements. The spatial marching approach has been directed towards derivation of approximate flow equations and development of an efficient solution algorithm suitable for computing impeller flow fields. Flow in a rotating 90-degree bend was used as a test case for the spatial marching approach. Computed results for the rotating duct show characteristic features of impeller flow fields.

20. DISTRIBUTION / AVAILABILITY OF ABSTRACT
☐ UNCLASSIFIED/UNLIMITED ☐ SAME AS RPT. ☐ DTIC USERS

21. ABSTRACT SECURITY CLASSIFICATION
Unclassified

22a. NAME OF RESPONSIBLE INDIVIDUAL

22b. TELEPHONE (Include Area Code)

22c. OFFICE SYMBOL

DD FORM 1473, 84 MAR

83 APR edition may be used until exhausted.
All other editions are obsolete.

SECURITY CLASSIFICATION OF THIS PAGE
UNCLASSIFIED

Introduction

Centrifugal impellers are used in a wide variety of applications. One of the primary advantages of centrifugal impellers is the high pressure ratios that can be achieved from a small sized machine. Compactness and lightweight design (by comparison with axial machines) enables vehicles in certain applications of interest to the Army, for instance in some automotive and helicopter applications, to deliver additional payload and/or to extend their range. However, losses and flow distortions in these machines are higher compared to an equivalent axial machine. Improvements in the efficiency of centrifugal impellers could come from a better understanding of the flow mechanisms in the impeller passage that are sources of losses and flow distortion.

State-of-the-art in centrifugal impeller design is a combination of experience, simple analyses with empiricism to estimate overall performance, and input from a database generated by experiments. In support of this approach the acquisition of experimental data from actual machines has been quite extensive. However, few fundamental experiments designed to isolate various effects inside the machines have been performed mainly because of the experimental difficulties and the high cost of making such measurements. Consequently the understanding of the fundamental fluid mechanics of centrifugal impellers has been rather poor. Computational approaches are an effective means of gaining this understanding of the physics of impeller flow fields. The development and utilization of computational tools to study impeller flow fields were pursued under the present contract.

Scope of the Study

The scope of the present study was to address the development and implementation of computational procedures for analysis and prediction of flows in centrifugal impellers. Two approaches have been investigated: (a) solution of the Navier-Stokes equations, and (b) solution of an approximate set of viscous primary/secondary flow equations by an efficient spatial marching algorithm.

Solution of the Navier-Stokes equations has been directed towards computing the flow field in a rotating centrifugal impeller passage. The advantage of using the Navier-Stokes equations is that they do not contain any approximations other than those associated with the use of a turbulence model. Flow in Eckardt's impeller [1] was used as a test case for the Navier Stokes solution procedure. The centrifugal compressor consisted of an impeller/vaneless diffuser combination. This set-up was advantageous for the present study, since the flow in the impeller could be computed and analyzed in isolation and compared with experimental data, without the additional complications caused by a vaned diffuser.

The spatial marching approach has been directed towards derivation of approximate flow equations and development of an efficient solution algorithm suitable for computing impeller flow fields. The primary advantage of the spatial marching procedure is that detailed resolution of the complex flow structure could be obtained economically utilizing very high density grids. For example, using 10^6 grid points, a spatial marching solution requires only about 20 minutes of CRAY-XMP run time, whereas a state-of-the-art Navier-Stokes code would typically require more than 10 hours of run time. Flow in a rotating 90-degree bend was used as a test case to develop approximate equations for impeller flow fields. This test case was also useful to study the effects of rotation and curvature on flow distortion in impellers.

An important element in the utilization of computational procedures for the impeller flow field is the ability to describe the geometry of the impeller and generate a suitable computational grid. A simple, effective algebraic grid generation procedure was developed to generate suitable computational grids to compute viscous flow fields in centrifugal impellers. Computational grids generated by the procedure could be utilized by both the Navier-Stokes and the spatial marching solution procedures.

The remainder of this report describes the development of generalized primary/secondary flow analysis for the study of flows in rotating passages and application of the Navier-Stokes solution procedure for the flow in a centrifugal impeller passage. Results obtained from the two solution procedures are discussed.

Generalized Primary/Secondary Flow Analysis

A unique spatial-marching solution procedure has been developed for computing three-dimensional viscous flows with a dominant flow direction, such as impeller passage flows. The procedure is based on solution of the generalized primary/secondary flow equations which are an approximation to the Navier-Stokes equations. Reference 2 contains a description of the generalized primary/secondary flow equations and an efficient solution procedure to solve these equations. Validation of the procedure for internal flow in a 90-degree bend duct is also described.

In the primary/secondary flow equations a small velocity vector is identified by velocity decomposition which provides a basis for approximating flows with large streamwise vorticity and secondary velocity. Two features of the primary/secondary flow equations central to identifying a small velocity vector for approximation are a locally specified primary-flow direction and a decomposition of the secondary velocity field. The local flow field velocity vector is expressed as a primary flow component in the primary-flow direction and a secondary flow component normal to this direction. The secondary velocity component is decomposed into components defined from a scalar-potential and a vector-potential. The vector-potential defines the streamwise vorticity and the secondary velocity component associated with the streamwise vorticity. The remaining scalar-potential component contribution can be assumed small in the transverse momentum equations, but is not otherwise neglected. This small scalar-potential approximation along with the viscous approximation neglecting streamwise diffusion is sufficient to establish a well-posed initial value problem, which can be solved far more economically than the Navier-Stokes equations. No approximations are introduced for pressure, the pressure field is computed in this approach. Typical run times for the method are on the order of 20 minutes for a computational grid of 10^6 points. These short run times allow refined grid solutions that resolve complex flow structures in three-dimensional viscous flows. The trade-offs for this advantage are that the approximations limit the range of flow problems that can be addressed relative to the Navier-Stokes equations because of factors such as flow separation, stagnation points, and transonic flow effects. Nevertheless, this approach is well-suited for a number of flows arising in practical situations and can provide a large number of detailed flow calculations at moderate cost for use in design optimization studies.

Flow in a rotating 90-degree bend was used as a model of a centrifugal impeller flow field and a test case for the spatial marching procedure. Figure 1 shows the geometry of the bend. A Reynolds number of 50,000 based on the passage width and a rotation number of 1 based on the tip radius and the inlet velocity were chosen as flow parameters. Potential flow streamlines through the non-rotating 90-degree bend were chosen as the local primary flow direction in the primary/secondary flow equations. Figure 2 shows the computed flow field at the exit of the bend. The vector plot of the secondary velocity field shows a complex flow pattern of interacting vortices. Associated with these vortices is distortion of the primary velocity field shown by contours of primary velocity. These contours show regions of high and low velocity, corresponding to vortex core locations, which contribute to the 'jet-wake' structure of the exit flow field; such exit flow structure is typical of rotating passages. Contours of the computed pressure field show a large pressure gradient across the passage which would correspond to blade loading in an impeller. The pressure field also shows distortion on the suction side of the passage due to the secondary flow vortices. The dominant effect of rotation of the passage on the exit flow field is evident when the computed exit flow field in Figure 2 in compared with the exit flow field from the same passage with no rotation (Reference 2, Figure 9).

Figures 3, 4, and 5 show the development of the flow field in the rotating passage. Unlike the non-rotating passage (Reference 2, Figures 5-10), there is no flow symmetry in the rotating passage. In the non-rotating passage the pressure gradients are due to the curvature of the bend whereas in the rotating passage Coriolis and centrifugal forces are the dominant effect on the pressure field. Note that this dominant effect of rotation on the pressure field is computed from the generalized primary/secondary flow equations even though the approximations are based on potential flow streamline directions in the non-rotating passage. Further, the computed pressure field is utilized in the flow computations without approximation. Vector plots of the secondary velocity field show the development of strong secondary flow vortices in the passage. The vortices are strongest at the exit of the passage where the effects of rotation are the largest. This contrasts with flow development in the non-rotating passage where the secondary flow vortices begin to decay at the exit of the passage. Associated with the development of the secondary flow and pressure fields is distortion of the primary velocity field. Interaction of the secondary flow vortices produces regions of high and low primary velocity. Primary velocity development in the rotating and non-rotating passages are different corresponding to the effects of rotation on the pressure and secondary velocity fields. Figure 6 compares the development of the primary velocity field in the rotating 90-degree bend with the measured meridional velocity development in Eckardt's impeller [1]. The computed primary velocity development in the rotating bend shows all the flow features of the measured meridional velocity development in the centrifugal impeller. This would indicate that the character of the flow field in the impeller is dominated by primary/secondary flow interaction generated by the effects of rotation and curvature. Further, these effects are correctly predicted by the generalized primary/secondary flow equations.

Figure 7 compares the exit flow field computed with the generalized primary/secondary flow equations with that obtained by pressure approximations [3]. In spatial marching methods based on pressure approximations, the streamwise pressure gradient is specified in the streamwise momentum equation. For the flow in the rotating bend, the streamwise pressure gradient was computed from the potential flow pressure distribution in the non-rotating bend. The computed flow fields at the exit of the passage are very different, as seen in Figure 7. Some of the differences could be attributed to utilizing streamwise pressure gradients from the non-rotating bend in the pressure approximation. Utilizing streamwise pressure gradients obtained from inviscid rotational flow in the rotating bend would require solution of the Euler equations. Such computations are expensive and would nullify the run time advantages of spatial marching methods over solution of the Navier-Stokes equations. Approximations in the generalized primary/secondary flow equations are based on a local primary flow direction. For the flow in the rotating bend, potential flow streamline directions in the non-rotating bend are an appropriate choice for the local primary flow direction and were shown in Figure 6 to predict a flow structure in qualitative agreement with that in Eckardt's impeller. These results demonstrate the important effect that different spatial marching approximations have on predicted flow behaviour.

Impeller Geometry and Grid Generation

The impeller under consideration is "rotor o" described by Eckardt [1]. This impeller has 20 blades, with blade camber lines that have ellipsoidal shapes in cylindrical sections. In terms of a cylindrical-polar coordinate system, n, θ, z (with z being the coordinate along the impeller axis), the blade camber lines can be described by a relation of the form $\theta = \theta(z)$. Hence, the intersection of an impeller blade with a plane normal to the impeller axis is a radial line. As a consequence, the impeller outflow angle is 90° (i.e. the impeller does not have any "backsweep").

The definition of the impeller is completed by a description of the hub and shroud contours. Given relations of the form $f(n, z) = 0$ for these contours, and

$\theta = \theta(z)$ for the blade camber lines, blade-hub and blade-shroud intersection lines can be constructed easily. If the blade thickness is neglected, then the passage between two adjacent blades forms a "duct" whose four corner lines are two sets of blade-hub and blade-shroud intersection lines. For the purpose of flow field computations, this blade passage duct is extended by a helical section upstream of the impeller inlet and a radial section downstream of the impeller exit.

The computational grid is now generated as follows. First, a "center-line" is defined as the "average" of the four corner lines of the impeller passage. A mesh point distribution is specified along this center-line (in the actual calculations, a uniform distribution has been used). At each mesh point on the center-line, a transverse plane is defined normal to the center-line. The intersection of this plane with the four corner lines of the impeller passage determines the four corners of a quadrilateral, which is used to approximate the shape of the cross-section of the duct. A mesh is then generated on this quadrilateral by constructing mesh point distributions on each of its four sides and connecting mesh points on opposite sides by straight lines. In the actual flow field calculations, the mesh points on the sides of the quadrilateral are clustered near the corners using Oh's technique [4]; the clustering is allowed to change with the cross-sections to properly resolve the boundary layers everywhere in the impeller passage.

Figure 8 shows the impeller geometry constructed as described above (without upstream and downstream extensions), and a set of 7 transverse plane grids in a blade passage (with extensions). For illustration purposes, the grids shown are coarse (14 x 14), but have mesh point clusterings near the corners similar to those in the fine grids used in the actual flow field calculations. Computational grids generated by the above technique could be utilized with the spatial marching and the Navier-Stokes solvers.

Navier-Stokes Analysis of Centrifugal Impeller Flow Fields

Solution of the flow field in Eckardt's impeller/vaneless diffuser [1] has been computed with the Reynolds averaged compressible Navier-Stokes equations. For the impeller, the governing equations are written in a rotating cylindrical coordinate system fixed to the impeller axis. The continuity equation is written as

$$\frac{\partial \rho}{\partial t} + \nabla \cdot (\rho \mathbf{U}) = 0 \tag{1}$$

The momentum conservation equation is

$$\frac{\partial (\rho \mathbf{U})}{\partial t} + \nabla \cdot (\rho \mathbf{U}\mathbf{U}) + 2\omega \mathrm{x} \mathbf{U} + \omega \mathrm{x} \omega \mathrm{x} \mathbf{r} = - \nabla p + \nabla \cdot \tau \tag{2}$$

where τ is the stress tensor (molecular and turbulence) given by

$$\tau_{ij} = 2\mu_{eff} \mathbf{e}_{ij} - 2/3\mu_{eff} \nabla \cdot \mathbf{U} \delta_{ij} \tag{3}$$

where the rate of the strain e_{ij} is given by

$$e_{ij} = 1/2 \left[\frac{\partial u_j}{\partial x_j} + \frac{\partial u_j}{\partial x_j} \right] \tag{4}$$

The effective viscosity μ_{eff} is the sum of the molecular and turbulent viscosities

$$\mu_{eff} = \mu + \mu_T \tag{5}$$

The turbulent viscosity μ_T is obtained from the turbulence model.

The energy conservation equation is written as

$$\frac{\partial (\rho h)}{\partial t} + \nabla \cdot (\rho \mathbf{U} h) = \frac{Dp}{Dt} - \nabla \cdot \mathbf{q} + \Phi \tag{6}$$

where Φ is the viscous dissipation per unit volume and q the heat flux vector.

The dissipation rate Φ is expressed as

$$\Phi = \mu_{eff} [2\mathbf{e}_{ij}\mathbf{e}_{ij} - 2/3(\nabla \cdot \mathbf{U})^2] \tag{7}$$

and the heat flux vector q is given by

$$q = -(\kappa + \kappa_T) \nabla T \tag{8}$$

where κ and κ_T are molecular and turbulent thermal conductivities, respectively. In the present analysis, κ and κ_T are obtained assuming constant molecular and turbulent Prandtl number Pr and Pr_T, i.e.,

$$\kappa = \frac{\mu C_p}{Pr} \tag{9a}$$

$$\kappa_T = \frac{\mu_T C_p}{Pr_T} \tag{9b}$$

A general non-orthogonal coordinate transformation to a body fitted grid is used to handle the complex geometry in the solution procedure. The governing equations are solved by a linearized Block Implicit (LBI) scheme [5]. The numerical scheme is implicit and computationally efficient. In the present application, three-point central differences are used in the transformed coordinate system, and artificial dissipation terms of the form

$$\frac{\partial}{\partial x_j} \left[(\mu_{art})_j \frac{\partial \phi}{\partial x_j} \right] \tag{10}$$

are added to the governing equations for each coordinate direction j. The variable ϕ denotes the velocity component U_i for the x_i-direction momentum equation, the density ρ for the continuity equation, and the enthalpy h for the energy equation. The coefficient $(\mu_{art})_j$ is obtained from

$$\rho U_j \nabla x_j \leq (1/\sigma_d)[\bar{\mu} + (\mu_{art})_j] \tag{11}$$

where ∇x_j is the grid spacing at the point in question. The quantity $\bar{\mu}$ denotes the effective viscosity (μ_{eff}) for the momemtum equations, (μ_{eff}/Pr) for the energy equation, (μ_{eff}/σ_κ) for the turbulence kinetic-energy equation, ($\mu_{eff}/\sigma_\epsilon$) for the turbulence dissipation equation, and is zero for the continuity equation. σ_d was chosen to be 0.5 for the present computations.

Figure 8 illustrates the impeller geometry and computational grid system. The previously described algebraic grid generation procedure was used to construct the computational grid. For clarity, only a few of the transverse planes and grid points are shown in Figure 8. A computational grid of 40 x 40 points in transverse planes and 120 streamwise stations was used for the solution. Grid points were clustered towards the hub, shroud and blade surfaces to resolve viscous shear layers.

Flow Parameters, Boundary Conditions, and Initial Conditions

Flow parameters were chosen to correspond to the design point of the impeller. No-slip wall conditions were prescribed on hub, shroud and blade surfaces. Further, the normal gradient of the temperature and reduced pressure were set to zero on the solid surfaces. At the inflow boundary, total temperature and flow angle were specified; total pressure was specified in the core inviscid region of the flow. Turbulent velocity profiles of prescribed boundary layer thickness, but normalized by a local freestream velocity were specified instead of total pressure within the shear layers. The normalizing freestream velocity was updated after each time step to reflect transient variation of mass flow rate. Static pressure was specified at the outflow boundary based on design point conditions. Other variables (pressure at inflow, velocity and temperature at outflow) were extrapolated. Circumferential periodicity of the flow was specified in the vaneless diffuser section. The shroud was assumed fixed to the blades and the relative motion between the shroud and the blades was not included in the present computation. This effect was expected to be confined to a very thin region in the vicinity of the shroud.

To start the solution procedure, initial values of flow variables were obtained from a simple one-dimensional isentropic flow analysis. Flow was assumed to be along streamwise grid lines and the one-dimensional analysis was carried out for each of the streamwise grid lines. Near solid surfaces the velocity field was scaled by a specified turbulent boundary layer profile.

Turbulence Model

A simple mixing length type eddy viscosity model was used in the computations. Distributions normalized by a local freestream mixing length and modified to account for near-wall damping were specified. The local freestream mixing length is proportional to a local shear layer thickness distribution which was specified. Distances were computed from the grid point under consideration to the nearest wall. All of the boundary layers were assumed to be turbulent from the initial station.

Results

Figure 9 shows contours of the computed streamwise velocity in the impeller. The streamwise velocity component is nominally aligned with the impeller passage and in the rotating coordinate system fixed to the impeller. The velocity contours at the inlet show helical inflow to the impeller. This helical inflow corresponds to uniform axial velocity at the impeller inlet in the absolute coordinate system. Flowfield development shows the formation of a vortex (low velocity region) in the shroud/blade suction surface corner. The flow field also shows a second vortex with a high velocity core at the blade suction surface/hub corner. Similar flow development was described previously for the rotating bend. Such secondary flows are typical of impeller flow fields and is caused by rotation and curvature of the impeller passage. The distortion of the flow field by the secondary flow vortices is often referred to as the 'jet-wake' structure of the exit flow and is a source of high losses. Figure 10 compares the computed streamwise velocity development with measurements [1]. Computational grid planes closest to the experimental measurement stations were chosen for the comparison . The structure of the computed flow field compares well with measurements, showing correctly the regions of low and high velocities corresponding to the secondary flow development in the impeller passage.

Figure 11 and 12 show particle traces in the computed flow field to provide a visualization of the nature of impeller flows. Figure 12 is an enlargement of Figure 11. Particle traces which start in the blade pressure surface boundary layer show flow riding up the pressure surface towards the shroud, due to centrifugal forces. On reaching the shroud, the flow crosses the shroud and moves towards the suction surface due to the passage pressure gradient, and rolls up into a vortex at the shroud/suction surface corner. Flow in the shroud boundary layer merges with the flow from the pressure surface and rolls up into the same vortex. Some of the flow in the suction surface boundary layer rides up the suction surface in a manner similar to the pressure surface and rolls up into the vortex on the shroud/suction surface corner. Flow in suction surface boundary layer close to the hub rolls up into a vortex at the hub / suction surface corner along with hub boundary layer flow migrating from the pressure surface towards the suction surface. Fluid in the hub/pressure surface corner remains in the hub/ pressure surface corner at the exit of the impeller.

Figure 13 shows contours of the computed pressure field on the hub, mid-span, and shroud surfaces. The overall pressure field shows pressure rise through the impeller due to the work done by the impeller on the fluid. For this particular impeller design most of the pressure rise occurs in the latter half of the passage. Contours of the pressure field show pressure gradients across the width of the impeller passage corresponding to the blade loading. The blade loading is similar at all three sections shown in Figure 13. Figure 14 compares contours of the computed pressure on the shroud surface with measurements. The overall pressure distribution and loading at the shroud is well predicted by the computations.

Summary and Conclusions

Two computational procedures have been developed for analysis and prediction of flows in centrifugal impellers: (a) solution of the Navier-Stokes equations, and (b) solution of the generalized primary/secondary flow equations by an efficient spatial marching algorithm. Solutions obtained from the two procedures have provided useful insight into the structure of the three-dimensional viscous flow impellers.

Generalized primary/secondary flow equations have been derived which are applicable to flow in rotating passages. A spatial marching algorithm has been developed to solve the primary/secondary flow equations to obtain run time advantages over solution of the Navier-Stokes equations. Turbulent flow in a rotating 90-degree bend has been computed with the generalized primary/secondary flow equations. The computed flow field development in the bend is similar to the measured flow field development in Eckardt's impeller. The computed results also show the dominant effort of rotation on secondary flow development and flow distortion in the rotating passage.

A simple algebraic grid generation procedure has been developed to describe impeller geometries and generate suitable computational grids for viscous flows. The computational grids generated could be utilized by both the spatial marching and Navier-Stokes solution procedures.

The flow field in Eckardt's impeller has been computed by solution of the Navier-Stokes equations. Computed flow field development in the impeller compares well with measurements. These results also provide insight into the origins and development of the secondary flow structure in the impeller and the consequent flow field distortion at the exit of the impeller. Computed pressure on the shroud also compares well with measurements.

The computational procedures developed here would be very useful as tools in the analysis and design of centrifugal impellers. The procedures could be utilized in the analysis of the flow field in a impeller so as to suggest design modifications that would improve performance. The spatial marching procedure could be utilized in parametric studies of the effect of design parameters on the flow field in impellers. These studies could be carried out in simplified geometries (if necessary) that retain the essential features of the design.

Acknowledgements

The authors would like to thank Mr. R.C. Buggeln and Dr. H.J. Gibeling for their suggestions during the course of this work.

References

1. Eckardt, D.: Detailed Flow Investigations Within a High Speed Centrifugal Compressor Impeller, ASME Journal of Fluids Engineering 98, pp. 390-402.
2. Govindan, T.R., Briley, W.R. and McDonald, H.: Generalized Three-Dimensional Viscous Primary/Secondary Analysis, to be published AIAA J. (also SRA Reports R87-1 and R87-2).
3. Levy, R., Briley, W.R. and McDonald, H.: Viscous Primary/Secondary Flow Analysis for Use with Non-Orthogonal Coordinate Systems, AIAA Paper 83-0556, 1983.
4. Oh, Y.H.: An Analytical Transformation Technique for Generating Uniformly Spaced Computational Mesh, Final Report, NASA Langley Research Grant NSF 1087, Oct. 1978.
5. Briley, W.R. and McDonald, H.: On the Structure and Use of Linearized Block Implicit Schemes, J. Comp. Phys., Vol. 34, No. 1, pp. 54-72, January 1980.

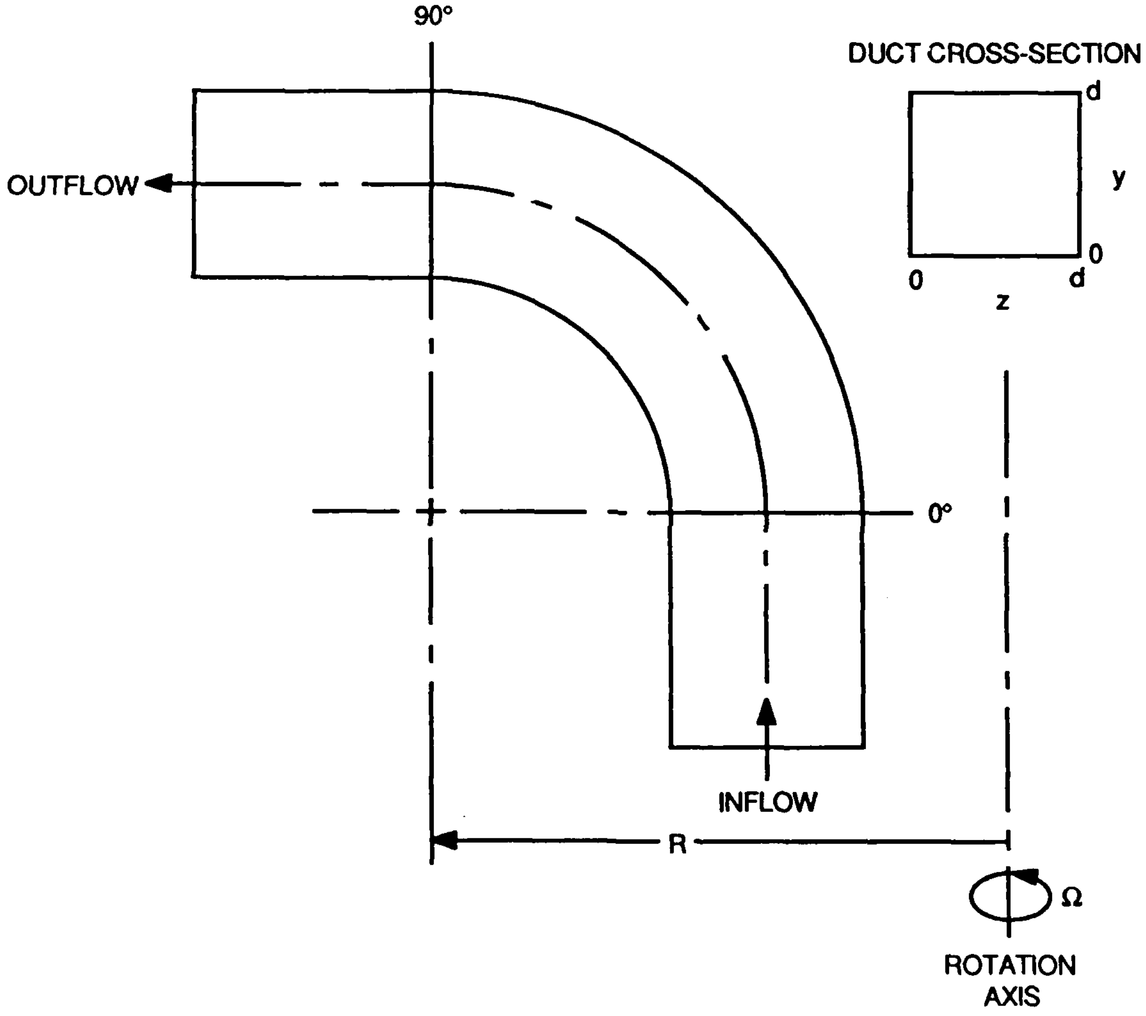

Figure 1. Geometry of the Rotating 90-Degree Bend.

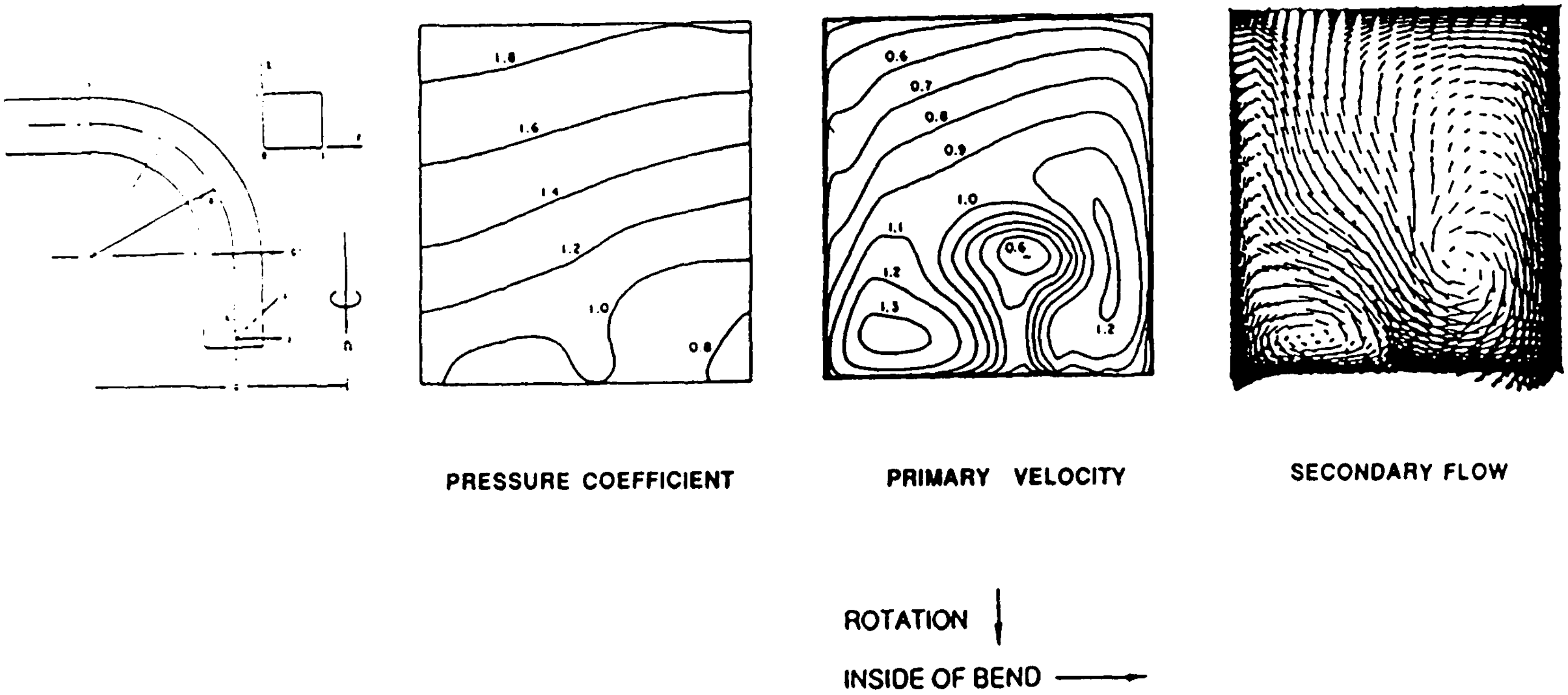

Figure 2. Computed Exit Flow in the Rotating Bend.

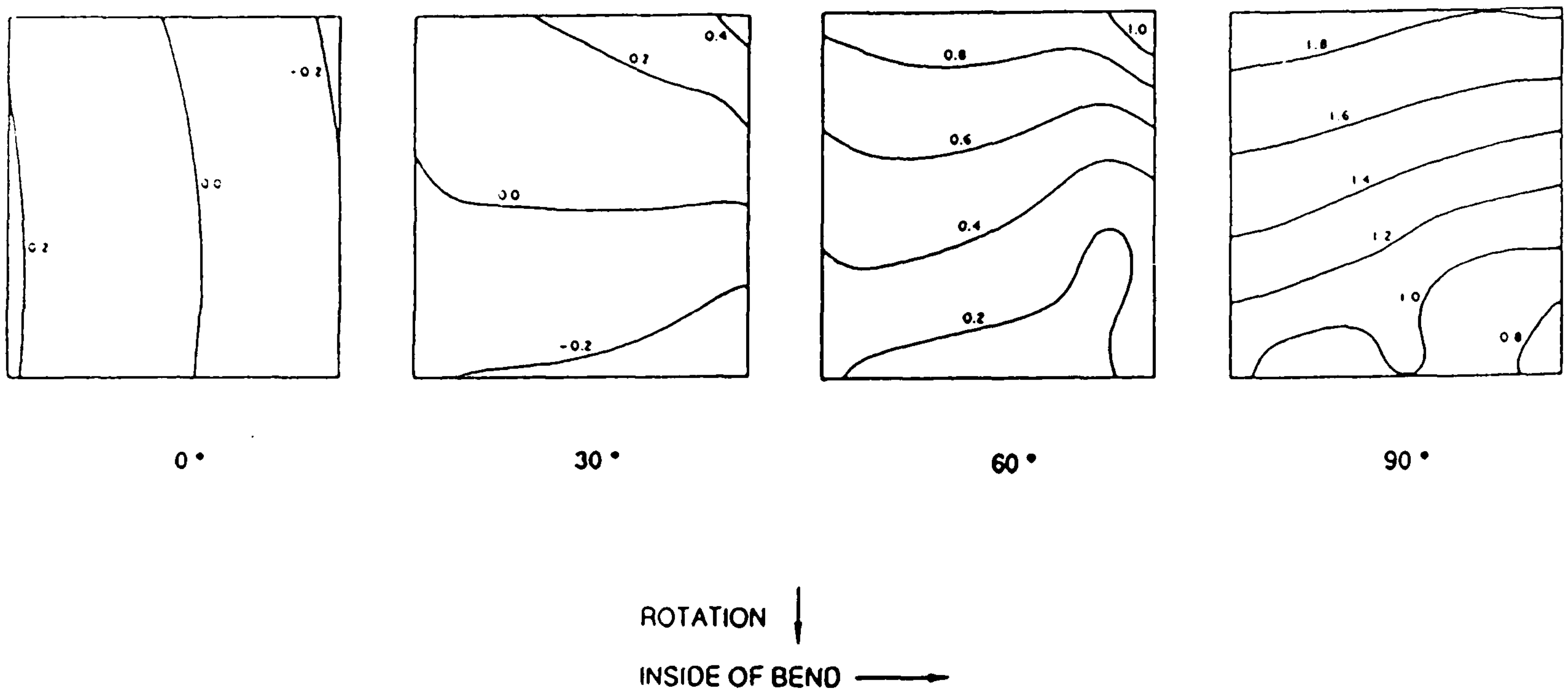

Figure 3. Computed Pressure Field Development in the Rotating Bend.

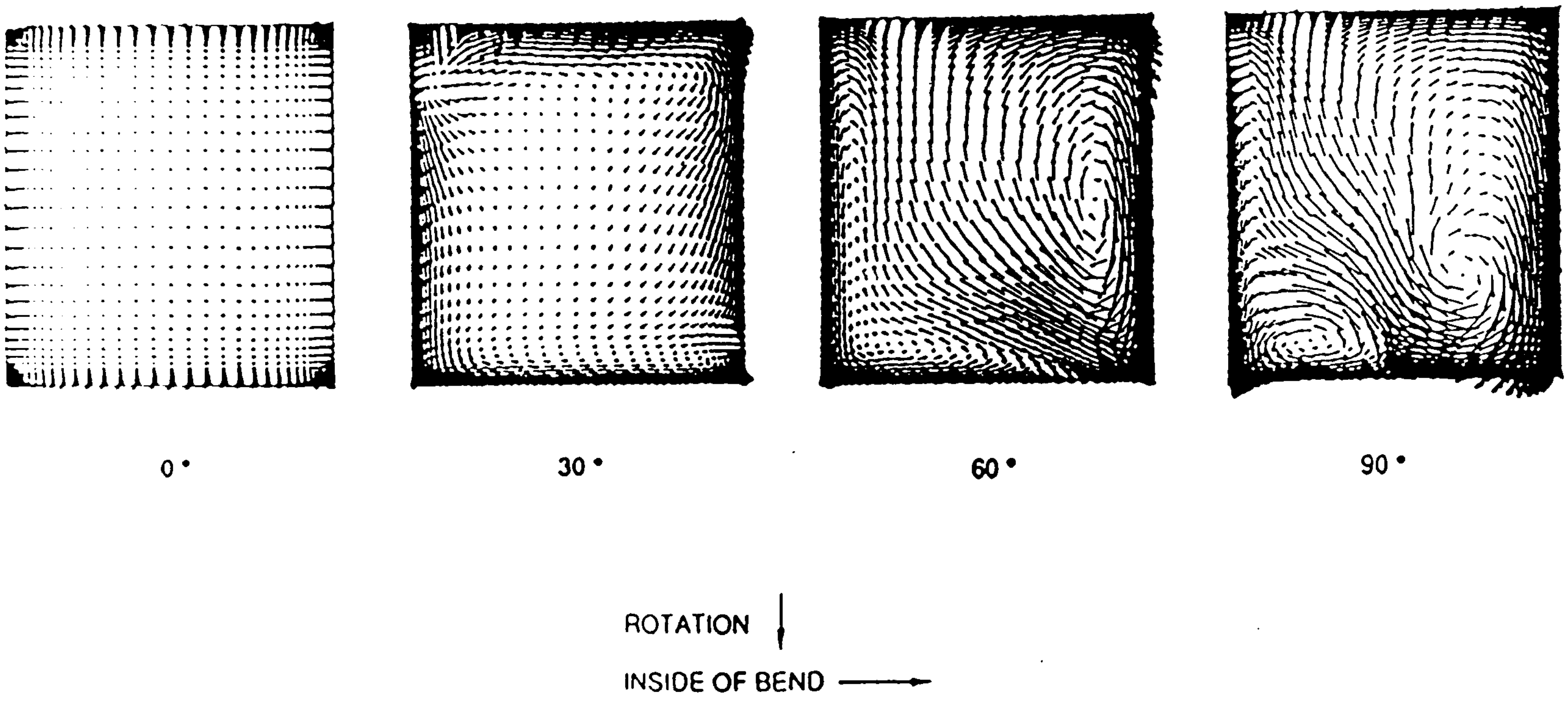

Figure 4. Secondary Flow Field Development in the Rotating Bend.

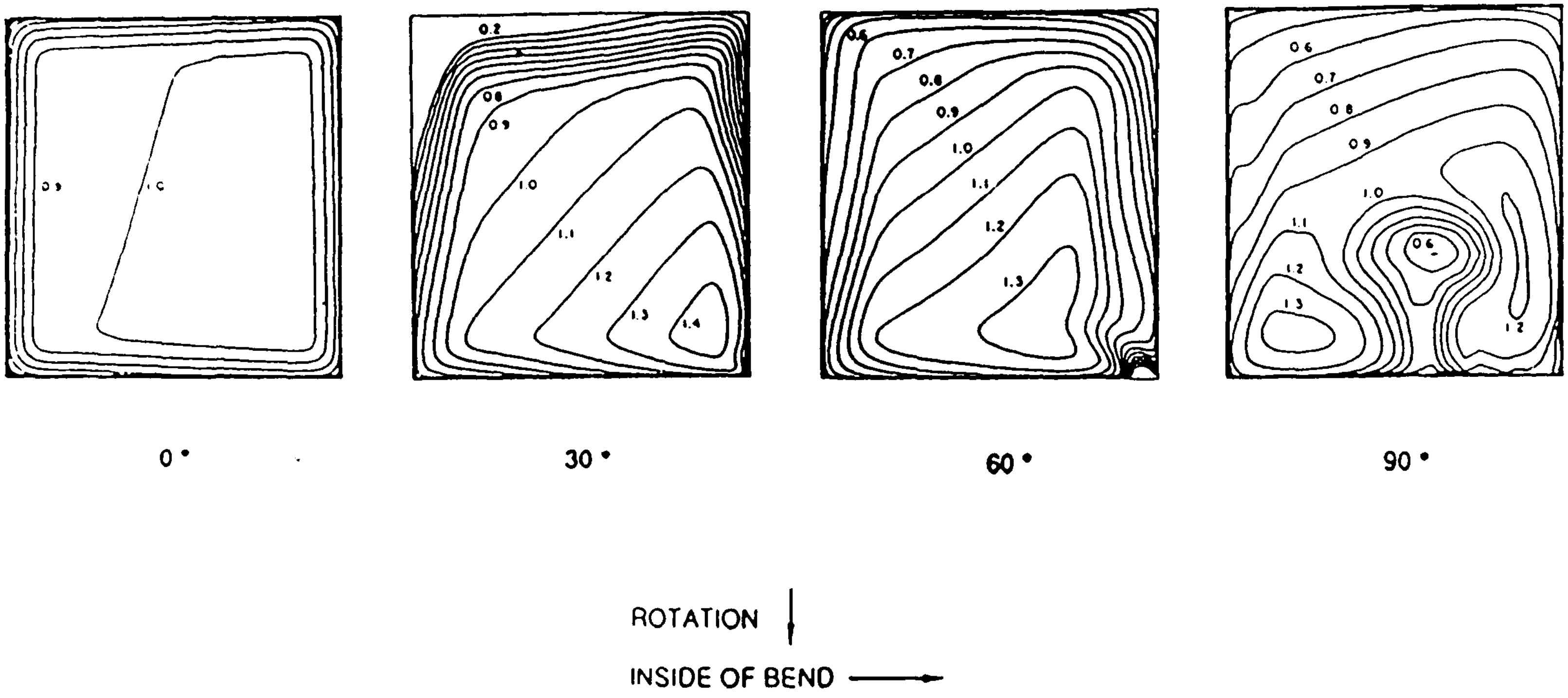

Figure 5. Primary Velocity Development in the Rotating Bend.

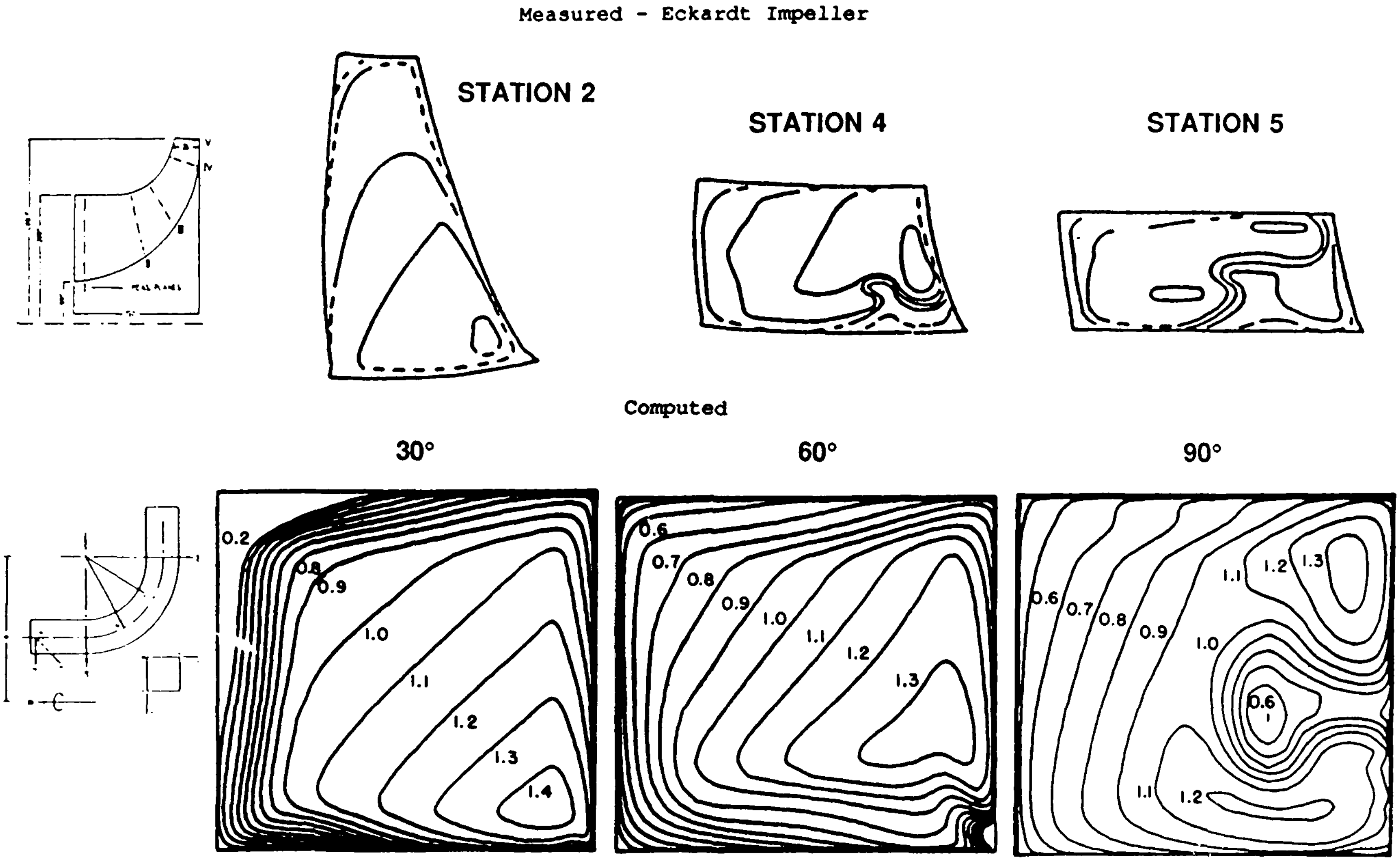

Figure 6. Comparison of the Computed Primary Velocity in the Rotating Bend with Measurements in Eckardt's Impeller.

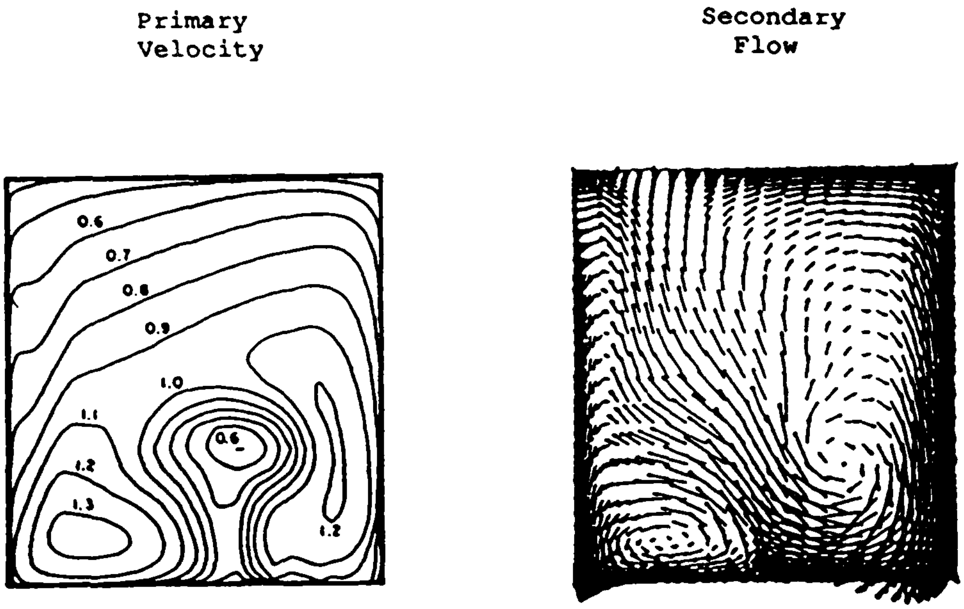

Primary
Velocity

Secondary
Flow

Primary/Secondary Flow Equations

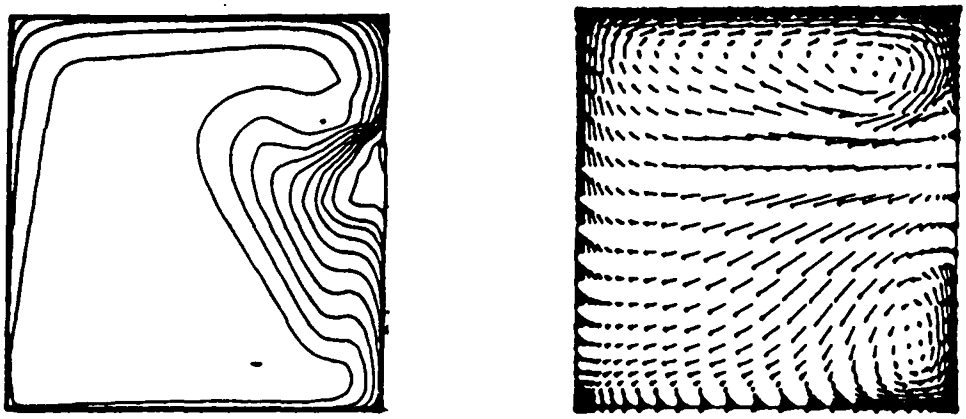

Pressure Approximations

Figure 7. Effect of Approximations on the Computed Flow Field in the Rotating Bend.

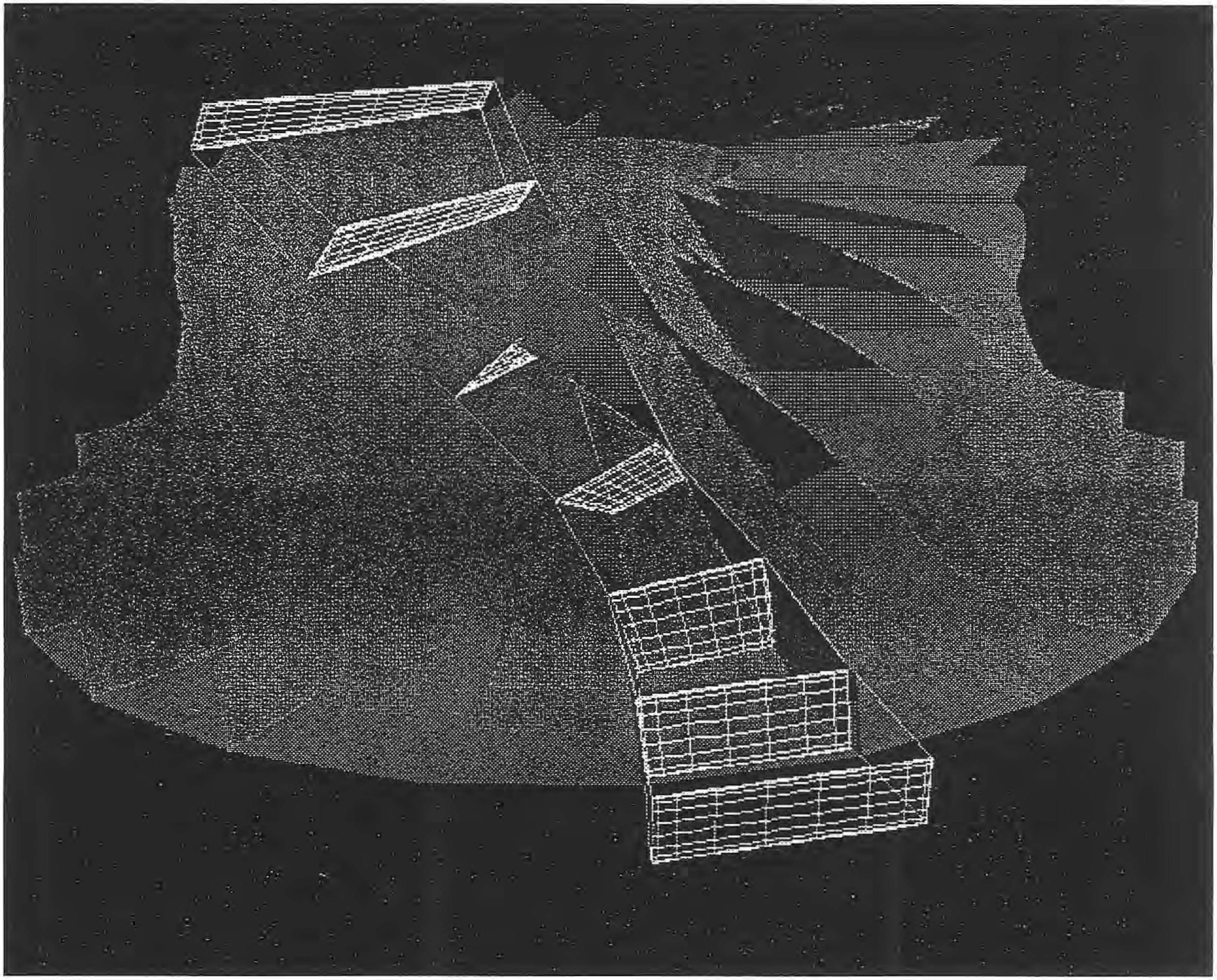

Figure 8. Geometry and Computational Grid for Eckardt's Impeller.

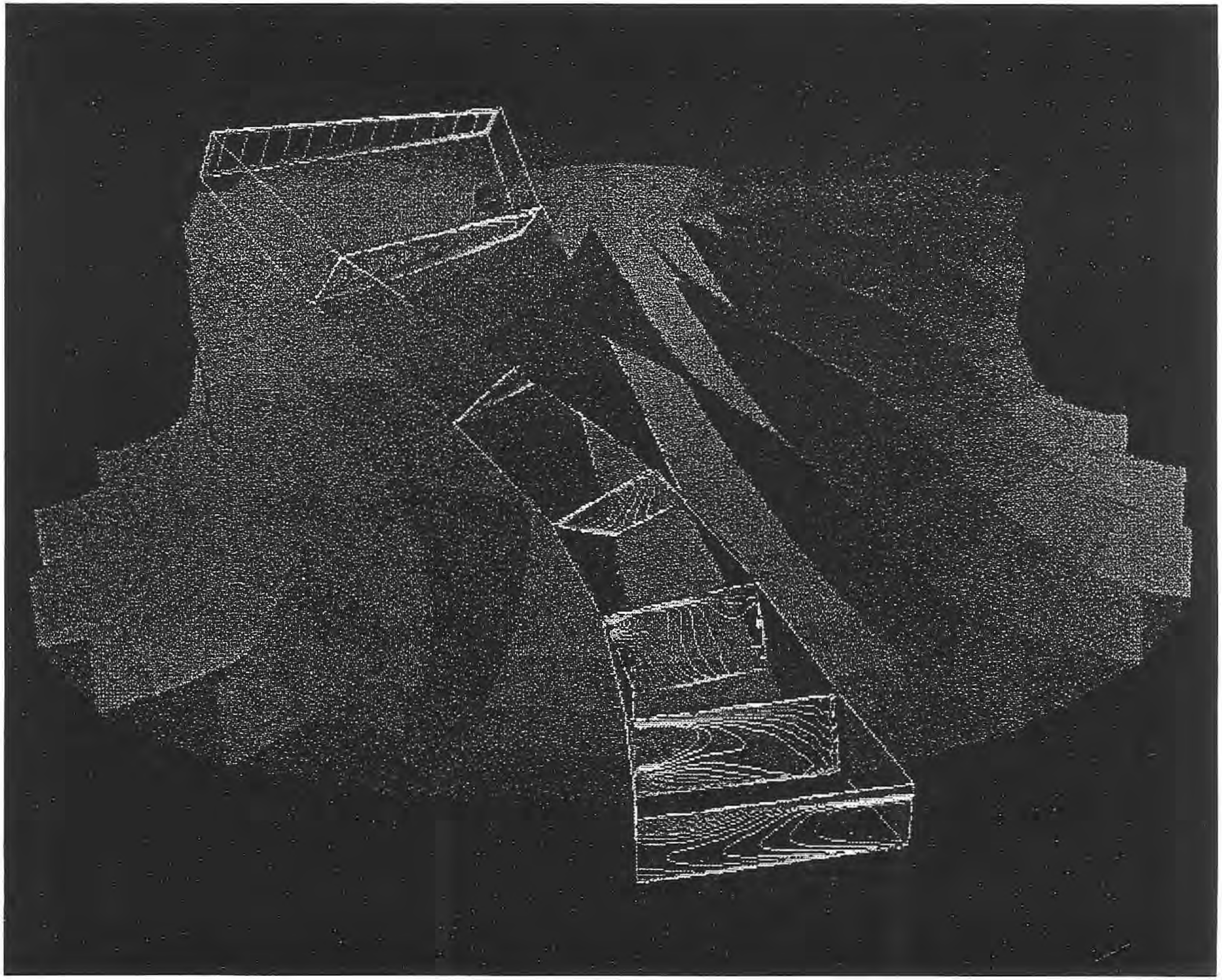

Figure 9. Contours of Computed Streamwise Velocity.

Measured - Eckardt Impeller

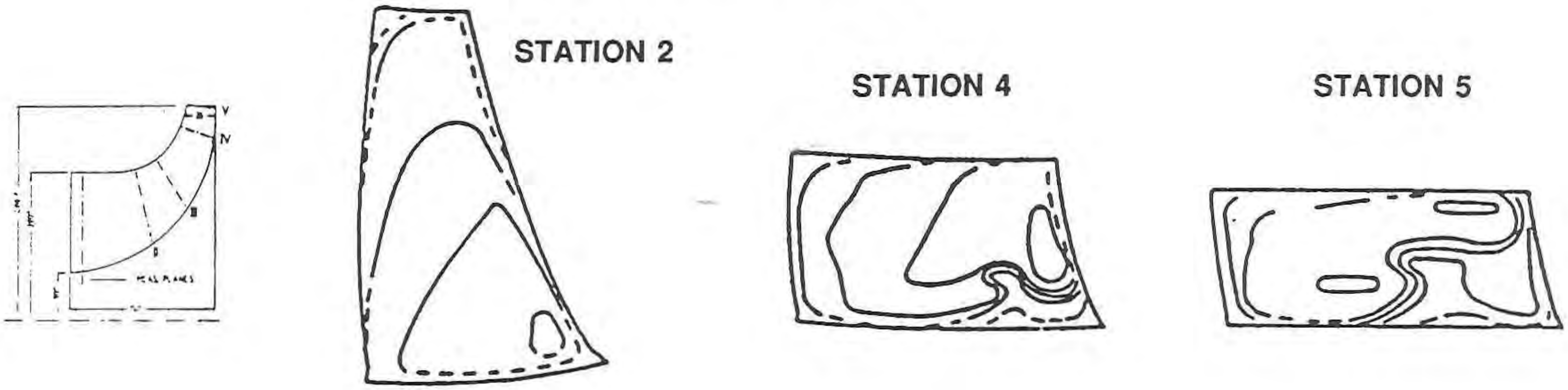

Computed

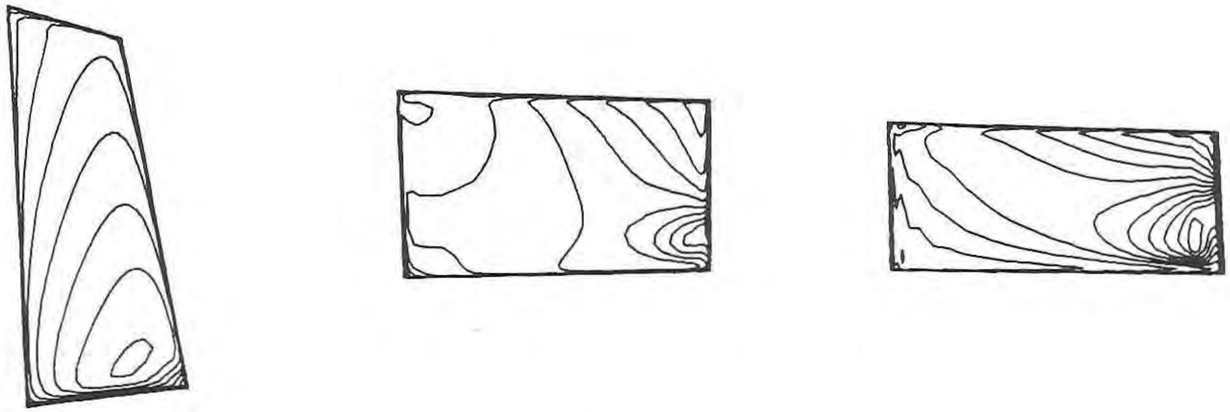

Figure 10. Comparison of Computed and Measured Streamwise Velocity in Eckardt's Impeller.

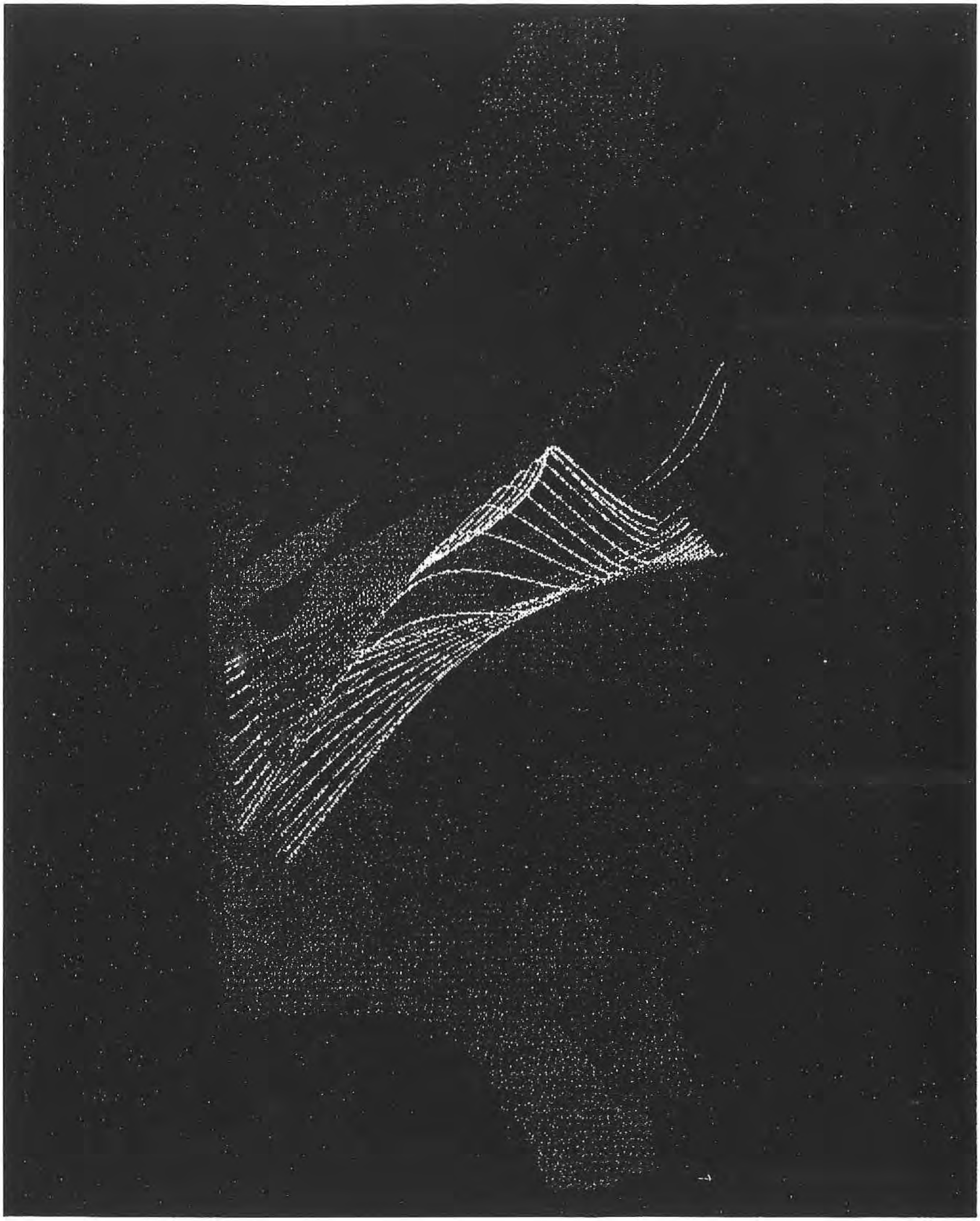

Figure 11. Particle Traces showing Secondary Flow Development.

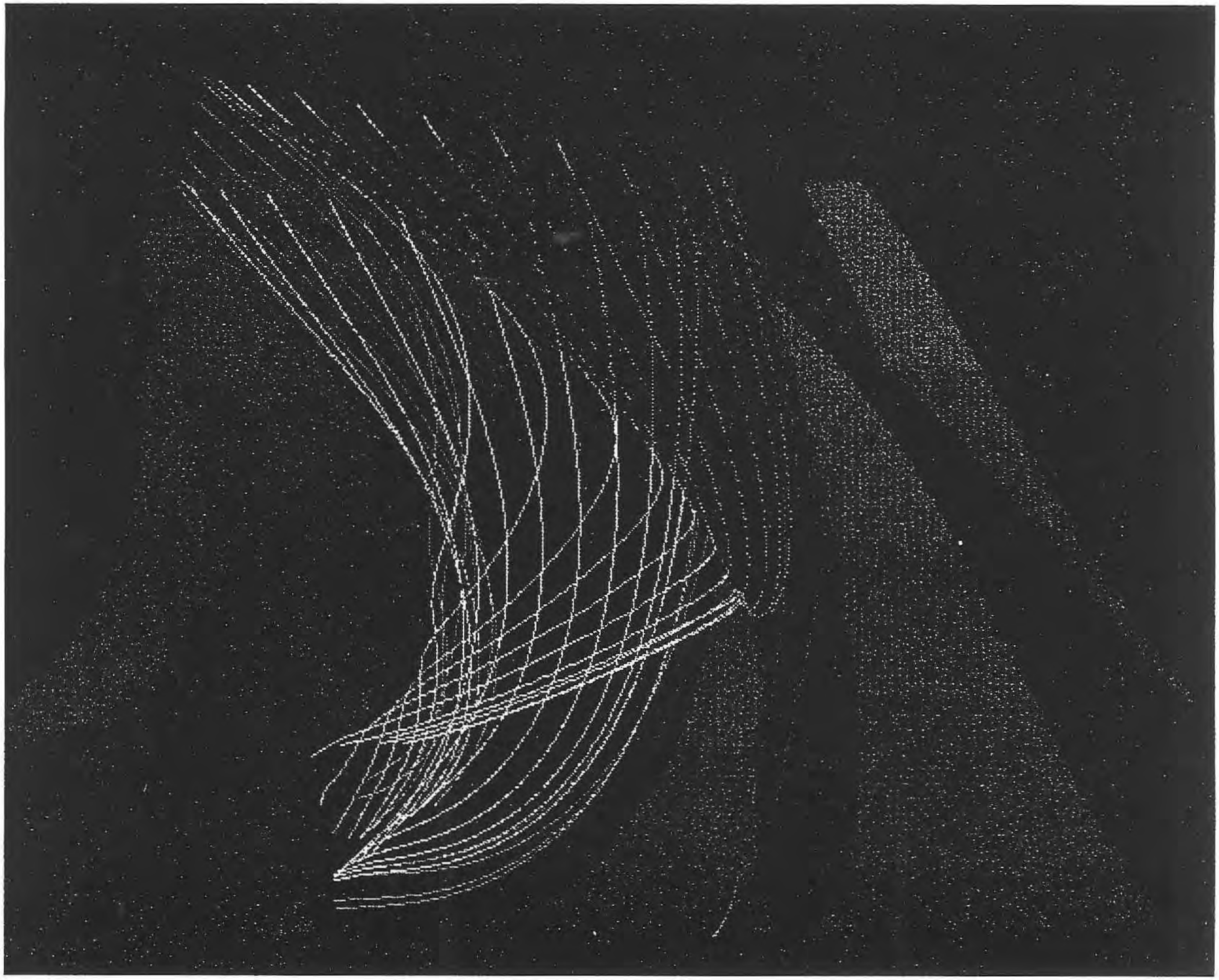

Figure 12. Particle Traces (Enlarged View).

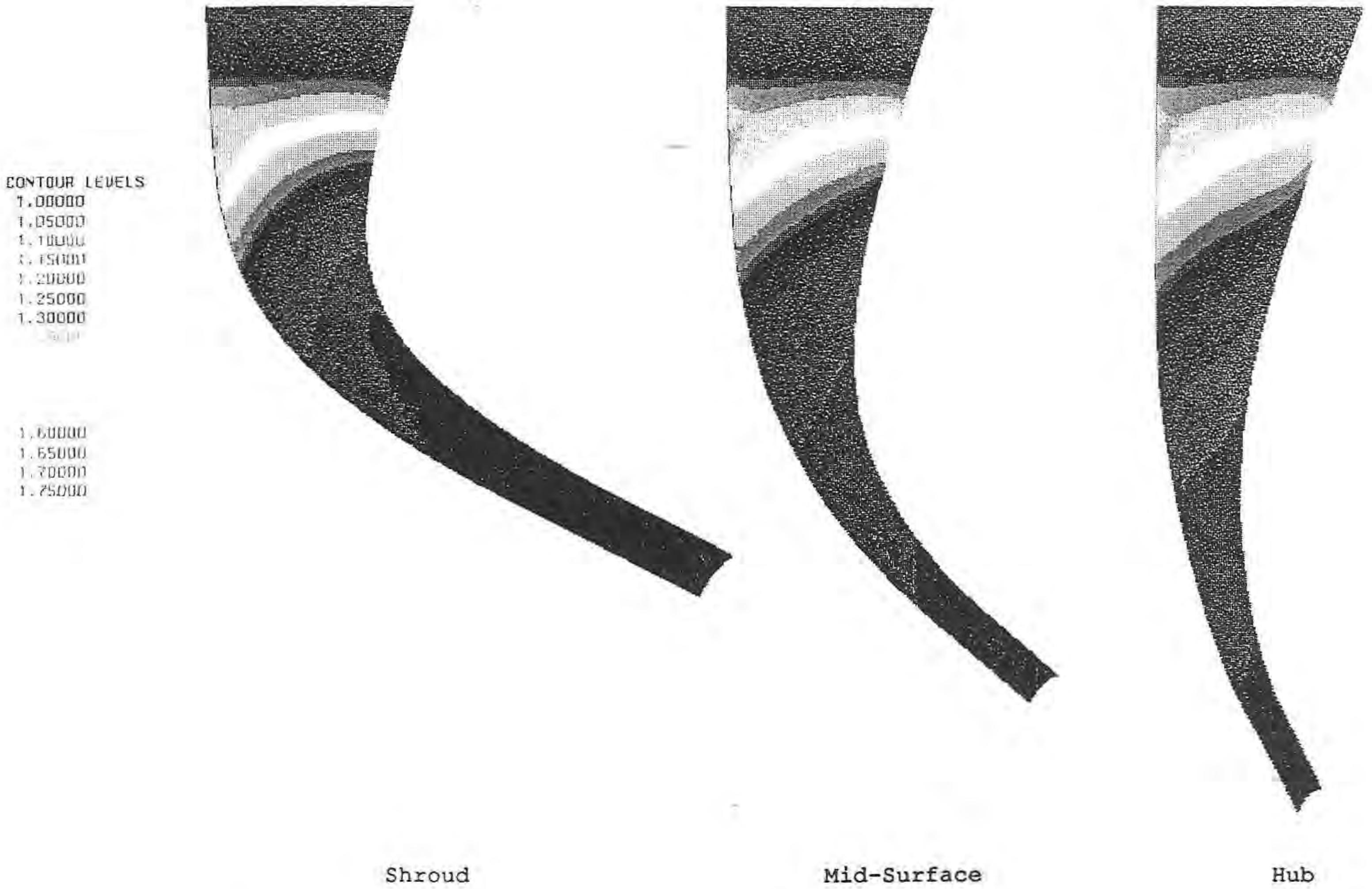

Figure 13. Computed Pressure Field in the Impeller.

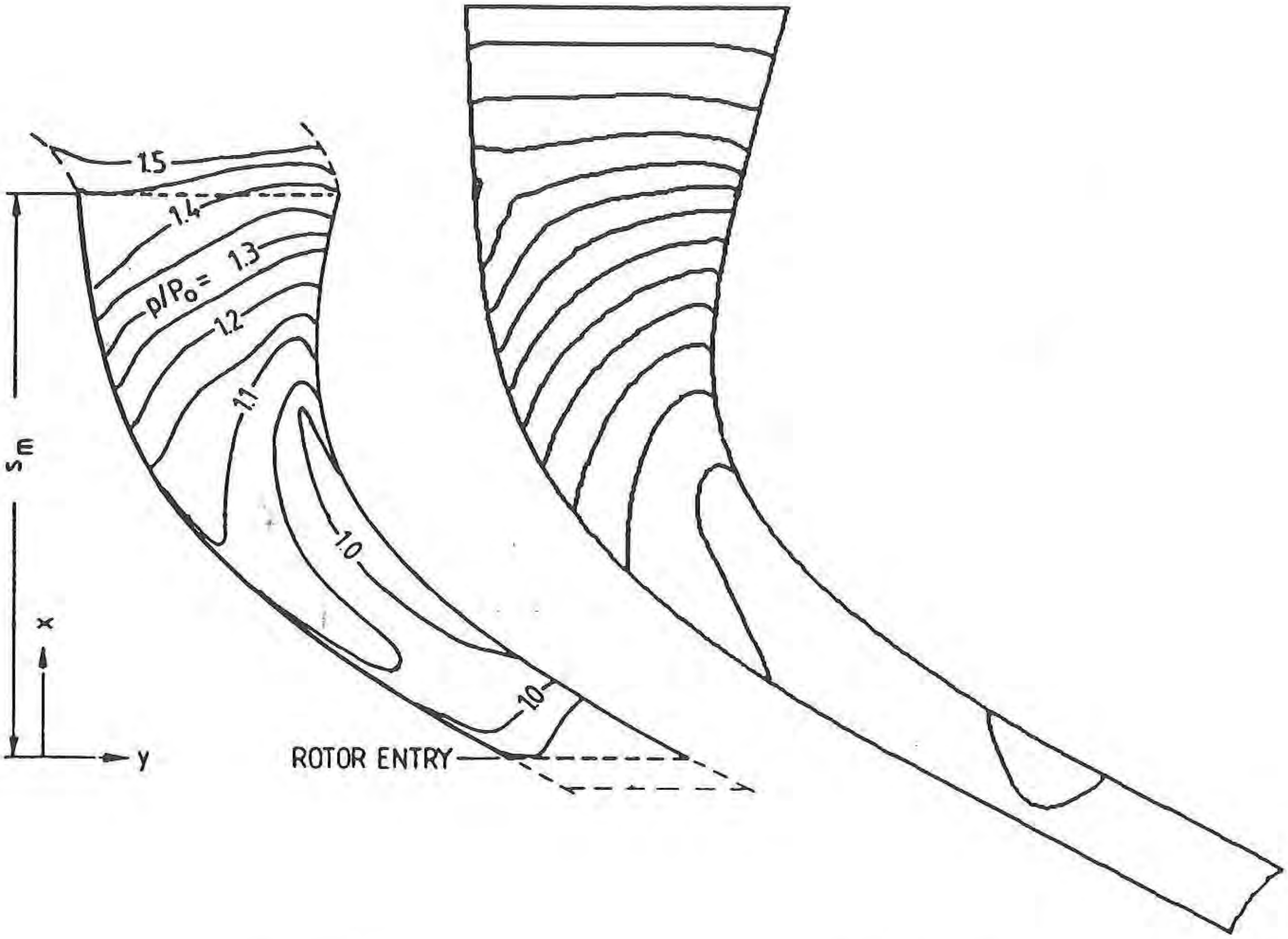

Measured

Computed

Figure 14. Comparison of Computed and Measured Pressure in the Shroud.